This is the peer-reviewed, final accepted version for American Mineralogist, published by the Mineralogical Society of America.
The published version is subject to change. Cite as Authors (Year) Title. American Mineralogist, in press.
DOI: https://doi.org/10.2138/am-2022-8502. http://www.minsocam.org/

Revision 1; Word Count: 6765 (excluding cover letter, abstract, reference list, tables and figures)

Low-temperature crystallography and vibrational properties of rozenite ($FeSO_4 \cdot 4H_2O$), a candidate mineral component of the polyhydrated sulfate deposits on Mars

Johannes M. Meusburger[1,2,3], Karen A. Hudson-Edwards[1], Chiu C. Tang[2], Eamonn T. Connolly[2], Rich A. Crane[1], A. Dominic Fortes[3*]

[1] Camborne School of Mines and Environment and Sustainability Institute, Tremough Campus, University of Exeter, Penryn TR10 9EZ, UK
[2] Diamond Light Source, Harwell Science and Innovation Campus, Fermi Avenue, Didcot OX11 0DE, UK
[3] ISIS Neutron and Muon Source, STFC Rutherford Appleton Laboratory, Harwell Science and Innovation Campus, Chilton, Didcot, Oxfordshire, OX11 0QX, UK
*corresponding author

Email addresses: JMM: johannes.meusburger@stfc.ac.uk KHE: k.hudson-edwards@exeter.ac.uk CCT: chiu.tang@diamond.ac.uk
ETC: eamonn.connolly@diamond.ac.uk RAC: r.crane@exeter.ac.uk ADF: dominic.fortes@stfc.ac.uk

Abstract:

Rozenite ($FeSO_4 \cdot 4H_2O$) is a candidate mineral component of the polyhydrated sulfate deposits on the surface and in the subsurface of Mars. In order to better understand its behavior at temperature conditions prevailing on the martian surface and aid its identification in ongoing and future Rover missions we have carried out a combined experimental and computational study of the mineral's structure and properties. We collected neutron powder diffraction data at temperatures ranging from 21 – 290 K, room temperature synchrotron X-ray data and Raman spectra. Moreover, first-principles calculations of the vibrational properties of rozenite were carried out to aid the interpretation of the Raman spectrum. We found, in contrast to a recent Raman spectroscopic study, that there are no phase transitions between 21 and 290 K. We confirm the heavy atom structure reported in the literature (space group $P2_1/n$) to be correct and present, for the first time, an unconstrained determination of the hydrogen atom positions by means of high-resolution neutron powder diffraction, and report the complete crystal structure at 290 K and 21 K. The anisotropy of the thermal expansion of the lattice vectors is $\alpha_a : \alpha_b : \alpha_c = 1.00 : 2.19 : 1.60$ at 285 K. Subsequent analysis of the thermal expansion tensor revealed highly anisotropic behavior as reflected in negative thermal expansion approximately $\parallel \langle 101 \rangle$ and ratios of the tensor eigenvalues of $\alpha_1 : \alpha_2 : \alpha_3 = -1 : 3.74 : 5.40$ at 285 K. Lastly, we demonstrated how combining Raman spectroscopy and X-ray diffraction of the same sample material sealed inside a capillary with complementary first-principles calculations yields accurate reference Raman spectra. This workflow enables the construction of a reliable Raman spectroscopic database for planetary exploration, which will be invaluable to shed light on the geological past as well as in identifying resources for the future colonization of planetary bodies throughout the solar system.

Keywords: polyhydrated sulfates, Mars, rozenite, negative thermal expansion, Raman spectroscopy, Density Functional Theory, Neutron Diffraction, Synchrotron Diffraction

Introduction

Ferrous iron sulfate minerals occur in various hydration states, $FeSO_4 \cdot nH_2O$ with n = 1, 4, 5, 6, 7, most commonly in the vicinity of sulfide ore deposits (Jambor et al. 2000). In such environments, weathering of ore and waste materials releases oxidized iron and sulfur, as well as a wide range of potentially toxic elements, into nearby surface waters (Hudson-Edwards et al. 1999; Nordstrom 2011), which subsequently precipitate as hydrous ferric and ferrous sulfates. Widespread occurrences of minerals diagnostic to acid mine drainage environments have been identified on the martian surface using both surface (Klingelhöfer et al. 2004) and orbit (Carter et al. 2013) based measurements. These findings have been interpreted as evidence for the existence of acidic aquatic environments early in martian history (Squyres et al. 2004). In detail, it has been proposed that hydrated sulfate minerals on Mars are secondary minerals produced by the evaporation of fluids involved in the aqueous alteration of martian basalt (Tosca et al. 2005). In the Valles Marineris canyon system sulfate minerals occur in sandy stratified deposits, typically exposed in canyon walls, and lie stratigraphically above widespread clay-mineral deposits (Roach et al. 2010). This stratigraphic sequence records a transition from neutral-alkaline (clay-forming) to acidic (iron sulfate-forming) aqueous environments indicating a change in global climate from wetter to dryer conditions starting around 3.5 Gya (Bibring et al. 2006). Due to their apparent role as climatological archives a detailed mineralogical characterization of these sulfate deposits is essential in order to decipher the nature and drivers of changing environmental conditions during the planet's early history. However, attempts to assign any single mineral species to the spectral data acquired for the polyhydrated sulfate deposits have proven to be challenging. This is due to inherent difficulty in differentiating between the diffuse near-IR reflectance spectra of different sulfate phases in the range 0.35 – 5.1 μm (corresponding to the OMEGA spectrometer on-board the Mars Express orbiter (Langevin et al. 2006)) that is

typically measured from orbit, i.e., significant spectral similarities occur between sulfates of different chemical composition and degrees of hydration (Bishop et al. 2009).

Numerous studies have been carried out in order to identify candidate minerals for the polyhydrated sulfate phase. If these deposits indeed originate from the alteration of olivine in martian basalt, the polyhydrated sulfate phase as its weathering product would likely be an iron- or magnesium-bearing sulfate (Bibring et al. 2005) or a sulfate mineral of intermediate composition. Among the iron sulfates, Carter et al. (2013) noted that rozenite matched the data acquired by OMEGA and CRISM very well. Wang et al. (2016), however, observed by studying the phase stability of melanterite ($FeSO_4 \cdot 7H_2O$), under variable temperature and relative humidity conditions, that at 323 K rozenite merely occurs as a transient state and further dehydrates to szomolnokite ($FeSO_4 \cdot H_2O$). Based on this finding they concluded that rozenite is not stable under present day martian surface conditions. Nevertheless, we note that in the same study Wang et al. (2016) reported that even after around 2030 hours (number obtained from supporting information S4 in Wang et al. (2016)) of exposure to relatively dry air (i.e., 33 % relative humidity) rozenite did not reveal any signs of dehydration at temperatures as high as 294 K, which is well above a maximum ground temperature of 280 K measured by the Curiosity rover over the first 100 sols of data acquisition (Gómez-Elvira et al. 2014). Moreover, rehydration of szomolnokite to rozenite and melanterite was observed at a temperature of 298 K at a relative humidity of 65 % (Mitchell 1984). Hence, even if temperatures as high as 323 K have prevailed at any point in martian history (leading to the dehydration of rozenite or melanterite), the process may have been reversed under present day martian environmental conditions. Thus, rozenite should still be regarded as a promising candidate mineral for the polyhydrated sulfate phase.

In order to unambiguously confirm the absence or presence of rozenite in the martian polyhydrated sulfate deposits, in-situ analytical techniques such as X-ray diffraction or Raman spectroscopy are needed. Raman spectroscopy in particular has proven very effective in discriminating between various sulfate mineral species (Košek et al. 2017), and thus appears well suited to unravel the mineralogical phase composition of the polyhydrated sulfate phase. Raman spectroscopic investigations of the martian soil have recently become possible. NASA's Perseverance Rover, landing on the martian surface in spring 2021, as well as the ESA's Rosalind Franklin Rover, which will likely arrive on Mars in 2023, both feature Raman spectrometers (Rosalind Franklin: The Raman Laser Spectrometer (Rull et al. 2017); Perseverance: SuperCam (Wiens et al. 2020) and SHERLOC (Bhartia et al. 2021)) as part of their scientific payload.

Interestingly, Chio et al. (2007) observed an apparent splitting of Raman-active vibrational modes of rozenite, which they suggested might be indicative of two structural phase transitions (T_{crit1} = 240 – 190 K, T_{crit2} = 140 – 90 K). The first transition is well within the range of temperatures relevant to the martian surface. Although Raman spectroscopy is a powerful tool for the identification of polymorphic phase transitions, sharpening of closely-spaced vibrational modes at low-temperatures might be erroneously interpreted as splitting due to a phase transition.

With rozenite being one of the most promising candidates for the polyhydrated sulfate phase on the martian surface, there is an interest in revisiting these putative phase transitions by means of neutron diffraction in order to determine the structural stability of rozenite at temperatures relevant to the martian surface as well as to solve the crystal structure of any proposed low-temperature polymorphs. For this reason, we have studied herein the structural stability of $FeSO_4 \cdot 4D_2O$ at temperatures ranging from 290 K down to 21 K by means of high-

resolution time-of-flight (TOF) neutron diffraction. Furthermore, the samples used for the neutron diffraction have been perdeuterated for the explicit reason of avoiding the large incoherent scattering signal from ordinary ^{1}H, which produces a substantial background masking weak Bragg peaks. Use of ^{2}D virtually eliminates this background and allows for rapid acquisition of high-quality data.

Since subtle changes in relative humidity may cause hydrated sulfates to partially or completely re- or dehydrate (Wang et al. 2016), it is entirely possible that the rozenite sample studied by Chio et al. (2007) underwent a transformation in between the initial phase identification by X-ray diffraction and the subsequent measurements of its vibrational properties. In order to confirm that the Raman spectra reported by Chio et al. (2007) indeed corresponds to rozenite, we have carried out Raman spectroscopy and synchrotron X-ray diffraction, which is able to detect the smallest amounts (i.e., 0.1 wt% (Thompson et al. 2009)) of any contaminant phases. Such measurements have been complemented with ab initio calculations in order to further explore the vibrational properties of rozenite. This combined experimental and theoretical approach allows us to cast light on the structural stability of rozenite at martian surface temperatures and, therefore, will aid the identification of rozenite in future and ongoing Mars missions.

Methods

Synthesis and phase analysis

$FeSO_4 \cdot 7H_2O$ (Sigma Aldrich ACS reagent grade) was dehydrated under vacuum for 48 hours at 473 K to prepare anhydrous $FeSO_4$. A hot supersaturated solution of $FeSO_4$ in 0.5 M D_2SO_4 (Sigma Aldrich > 99 atom % D) was then cooled to room temperature in order to precipitate fine-grained $FeSO_4 \cdot 7D_2O$. The sealed container was stored for several years, during which time diurnal and seasonal temperature changes resulted in the fine-grained material

135 altering into a fully dense coarse crystalline material. $FeSO_4 \cdot 7D_2O$ crystals were then ground to a
136 powder under helium in order to prevent exchange of ^2D with atmospheric ^1H. The powder was
137 loaded into rubber-sealed glass jars containing a saturated solution of $MgCl_2$ in D_2O (Sigma
138 Aldrich > 99 atom % D), which buffered the relative humidity at 33 % (Greenspan 1977), and
139 kept at 280 K for 3 days. The sample was then transferred, again under helium, into the sample
140 holder used for the neutron diffraction experiments. This comprised an aluminum frame
141 surrounding a cuboid sample cavity of dimensions 18 × 23 × 10 mm (w × h × d), open at the
142 front and back. The rear opening was first covered with a vanadium foil window sealed by
143 indium wire; powder was then transferred into the sample holder and the front opening was
144 sealed with another vanadium foil window. Gadolinium and cadmium foils were used to mask
145 scattering from various aluminum and steel parts that might be exposed to the incident neutron
146 beam around the edges of the vanadium windows. A cartridge heater, used for temperature
147 control, and a RhFe thermometer were inserted into the aluminum frame of the sample container
148 either side of the sample.
149 The sample was mounted into a closed cycle refrigerator (CCR) at the High-Resolution Powder
150 Diffraction (HRPD) beamline, ISIS Neutron and Muon Spallation Facility, UK. This instrument
151 allows collection of neutron time-of-flight (TOF) data in various 100 ms-wide 'windows'; those
152 used in this study were 30 – 130 ms and 100 – 200 ms. In HRPD's highest resolution
153 backscattering detectors (2θ = 154 – 176°), these yield diffraction patterns covering *d*-spacings
154 from 0.65 – 2.60 Å and 2.20 to 3.90 Å, respectively. The latter is often best used for rapid phase
155 identification, even though the incident neutron flux is very low, since Bragg peaks are typically
156 fewer and better dispersed, whilst also being rather more intense than those at shorter *d*-spacings.

We could thus quickly confirm that the sample was mostly rozenite, but with a few weak Bragg peaks identified as melanterite, indicating that dehydration of the starting material was incomplete. Heating the sample to 305 K for 60 min and then 315 K for a further 20 minutes resulted in the complete transformation of melanterite to rozenite. At 315 K, however, the high temperatures also gave rise to slight further dehydration and the formation of szomolnokite. Therefore, we lowered the temperature again to 305 K and kept the sample at this temperature for a further 12 minutes to ensure the complete transformation from melanterite to rozenite in the final sample material. The diffraction patterns acquired during dehydration of the sample are provided in the supplementary data (Fig. s1). Rietveld refinement of the neutron diffraction pattern acquired at 290 K suggests that the final sample material consists of 93.5(1) wt% rozenite and 6.5(1) wt% szomolnokite.

Protiated $FeSO_4 \cdot 4H_2O$ for the synchrotron X-ray diffraction and Raman analysis was synthesized using the dehydration method stated above. We placed the reagent $FeSO_4 \cdot 7H_2O$ in a rubber sealed glass jar containing a saturated solution of $MgCl_2$ in H_2O for 3 days at around 290 K. Subsequently, the sample was loaded into a borosilicate glass capillary of 0.5 mm diameter. The loaded specimen and the rest of the sample material were used for Raman analysis.

TOF Neutron diffraction and Rietveld refinement

High resolution TOF neutron diffraction data were collected at temperatures ranging from 315 to 21 K upon cooling and warming. After the initial dehydration at 305 and 315 K, the sample was cooled to 290 K. Datasets with long counting times of 3 h 17 min in the 30 – 130 ms and 100 – 200 ms TOF window were then collected to allow crystal structure refinement. In order to characterize the thermal expansion of rozenite, diffraction patterns with shorter counting

times of 50 min were collected on cooling in 10 K increments in the 100 – 200 ms TOF window in the temperature range from 290 – 21 K. At the base temperature of 21 K, another dataset for structural refinement was acquired in the 100 – 200 ms TOF window, again, for 3 h 17 min and in 30 – 130 ms window for 4 h 6 min. Lastly, we collected diffraction patterns upon heating from 35 – 285 K in 10 K increments for 37 min each. To ensure good thermal equilibrium between the heated aluminum frame of the sample holder and the powder sample itself, temperature changes were done at 3 K min^{-1} and a dwell time of 10 minutes after reaching a set-point was used prior to the start of data collection.

The data were time-focused, normalized to the incident spectrum and corrected for instrument efficiency using a V:Nb standard. Diffractometer calibration constants and instrumental peak-profile coefficients were determined using NIST silicon SRM640e and CeO_2 standards.

All refinements were carried out using the Rietveld method (Albinati and Willis 1982; van Laar and Schenk 2018) as implemented in the GSAS/EXPGUI software suite (Toby 2001). The diffraction patterns collected in HRPD's backscattering detector bank at 290 K and 21 K are displayed in Fig. 1 and the refinement parameters are given in Tab. 1 as well as in the CIF. Clearly, the refined structural models are in excellent agreement with the observed intensity data.

Unit-cell parameters were refined from the shorter 100 – 200 ms TOF datasets using initial least-squares cycles of Rietveld refinement, followed by a series of least-squares cycles using the 'F(calc) weighted' method; this workflow typically results in the most precise lattice parameters by virtue of fitting the intensities more accurately. For szomolnokite we used the structure reported by Talla and Wildner (2019) for the refinements and varied the lattice parameters and profile coefficients at each temperature. The small number of weak peaks

accessible in the 100 – 200 ms TOF window combined with the low symmetry of szomolnokite precludes us from following the evolution of the lattice parameters accurately as a function of temperature, which are therefore not reported in this study.

Synchrotron X-ray diffraction and room temperature Raman spectroscopy

A synchrotron X-ray powder diffraction pattern of the protiated rozenite capillary sample was collected at the I11 instrument, Diamond Light Source, UK using the Multi Analyzing Crystal detectors (Thompson et al. 2009). The experiment was carried out at an ambient temperature of 295 ± 0.5 K. The wavelength of 0.826574(9) Å and a zero-point error of 0.000315(2) ° was determined from a *NIST SRM 640c* silicon standard.

Raman spectra of protiated rozenite were acquired using a *B&WTek i-Raman Plus* spectrometer equipped with a neodymium doped Yttrium-Aluminum-Garnet laser that was frequency-doubled to 532 nm (maximum power of 30 mW as determined by the manufacturer). We collected data over the entire spectral range accessible to the spectrometer (i.e., 65 – 4200 cm^{-1}) with a resolution of smaller than 3.5 cm^{-1} (as determined by the manufacturer at 614 nm) on protiated rozenite powder samples both outside and inside of the very same borosilicate glass capillary that was used for the synchrotron diffraction analysis. The spectra were collected for 53 and 50 seconds and averaged over three acquisitions for the sample outside and inside of the capillary, respectively.

Ab initio vibrational properties from density functional theory (DFT):

We performed Kohn-Sham DFT calculations (Hohenberg and Kohn 1964; Kohn and Sham 1965) using ultrasoft pseudopotentials from the *GBRV* library (Garrity et al. 2014). Kinetic energy cut-off values and *k*-point grid density were derived from convergence testing; values of 70 Ry and 840 Ry were adopted for the wave function and charge density cut-offs, respectively

and a Monkhorst–Pack (Monkhorst and Pack 1976) *k*-point grid of $2 \times 1 \times 2$ was applied to sample the Brillouin zone.

The crystal structure as reported by Baur (1962) served as input geometry for an initial relaxation using the PBE functional (Perdew et al. 1996) in conjunction with the D2 dispersion correction (Grimme 2006). We have demonstrated in our previous work (Meusburger et al. 2021) that the PBE + D2 approach is very well suited to model geometries at temperatures close to the ground state both for dispersion-dominated solids as well as hydrogen-bonded solids such as the one under investigation.

The unit-cell and internal atomic coordinates were relaxed using the Broyden-Fletcher-Goldfarb-Shanno algorithm (Pfrommer et al. 1997), with convergence thresholds 1×10^{-6} Ry, 1×10^{-5} Ry/Bohr, 5×10^{-1} kbar for the total energy, forces, and pressure, respectively. Moreover, we applied a mixing factor of 0.3 and the local Thomas–Fermi charge mixing mode (Raczkowski et al. 2001) in order to achieve convergence in the self-consistent field cycles.

The structure optimized at the DFT + D level served as basis for the self-consistent computation of the Hubbard U by means of Density Functional Perturbation Theory (Timrov et al. 2018). The formulation of the Hubbard model following Dudarev et al. (1998) as well as nonorthogonalized atomic orbitals (Cococcioni and de Gironcoli 2005; Amadon et al. 2008) as projectors for the strongly localized 3*d* states of Fe^{2+} were used for all DFT + U calculations. We have tested multiple *q*-meshes and found that a grid of $2 \times 1 \times 2$ is necessary in order to derive Hubbard U values converged to within 0.0007 eV. Subsequently, we used the U value converged with respect to the *q*-mesh (i.e., 6.9806 eV), and again, computed the U value from this optimized structure. This procedure was repeated three times until the U value (i.e., 6.0156 eV) was identical with respect to the previous iteration.

This is the peer-reviewed, final accepted version for American Mineralogist, published by the Mineralogical Society of America.
The published version is subject to change. Cite as Authors (Year) Title. American Mineralogist, in press.
DOI: https://doi.org/10.2138/am-2022-8502. http://www.minsocam.org/

The geometry obtained from this workflow was then used as input for our phonon calculations at the Γ-point using Density Functional Perturbation Theory in order to compute the Infrared (IR) and Raman spectra of rozenite. The formalism of phonon calculations at the DFT + U level of theory as implemented in Quantum ESPRESSO's ph.x code is presented in detail in Floris et al. (2011, 2020). The open-source Quantum ESPRESSO code suite (Giannozzi et al. 2009, 2017) was used for all ab initio calculations. All files necessary to reproduce our calculations (i.e., input, output, and pseudopotential files) may be accessed on the MaterialsCloudArchive (Meusburger et al. 2022).

Results and discussion

Complete crystal structure and hydrogen bonding of $FeSO_4 \cdot 4D_2O$ at 290 K

The crystal structure of rozenite was first determined by Baur (1962) and consists of isolated cyclic $[Fe(H_2O)_4SO_4]_2$ units (Fig. 2a) interconnected by a hydrogen bond network (Fig. 2b). $[Fe(H_2O)_4SO_4]_2$ may be further divided into $Fe(H_2O)_4O_2$ octahedral units that engage in corner-sharing of O atoms with the SO_4 tetrahedral units (Fig. 2a).

Considering that the crystal structure of rozenite has not been revisited since its initial determination 60 years ago by means of single crystal X-ray diffraction, the results presented in this study improve the literature data substantially. In contrast to X-ray diffraction, which severely underestimates O – H bond lengths (Baur 1972), neutron diffraction is particularly well suited to accurately locate the hydrogen atom positions, allowing us to resolve long-standing ambiguities in the hydrogen bonding network of rozenite. In the following section the geometry of the octahedral and tetrahedral units will be discussed and compared to the structure reported by Baur (1962) (Tab. 2).

This is the peer-reviewed, final accepted version for American Mineralogist, published by the Mineralogical Society of America.
The published version is subject to change. Cite as Authors (Year) Title. American Mineralogist, in press.
DOI: https://doi.org/10.2138/am-2022-8502. http://www.minsocam.org/

Overall, the heavy atom (i.e., Fe, S, O) structure refined from the 290 K dataset is in excellent agreement with the structure reported by Baur (1962). This is reflected by the Mean Unsigned Differences (MUD)[1] of 0.011 Å (Fe – O bonds), 0.605 ° (O – Fe – O angles), 0.016 Å (S – O bonds) and (O – S – O angles) 0.76 ° being either well below or very close to the estimated standard deviations reported by Baur (1962) on the respective quantities.

Moving on to the hydrogen bond network it is noteworthy that Baur (1962) determined the heavy atom structure of rozenite and did not refine the position of the hydrogen atoms. Instead, he fixed the hydrogen atoms to the positions determined for the isotypic material $MgSO_4 \cdot 4H_2O$ (starkeyite) during the refinement process. As noted above, Baur (1962) determined the hydrogen atom positions by means of X-ray diffraction, which typically yields underestimated bond lengths as well as inaccurate H – O – H angles (Baur 1972). Baur (1962) counteracted this shortcoming by setting multiple constraints upon the hydrogen bond geometries. Therefore, we present for the first time the complete crystal structure of rozenite with all atomic positions derived from an unconstrained refinement. We assess the differences in the hydrogen bonding network and compare our results to the Baur (1962) study (Tab. 3).

The O ••• O contacts are in excellent agreement (MUD = 0.0168 Å, largest individual difference (LID) = 0.043 Å), which was expected since the distance of donor acceptor oxygens of the hydrogen bonding network is solely determined by the heavy atom positions. Despite the fact that X-ray diffraction (XRD) underestimates O – H bond lengths, the covalent O – H bond distances in our neutron diffraction and the Baur (1962) XRD study agree very well (MUD = 0.020 Å, LID = 0.063 Å). The reason for this is likely that the bond-length constraints for O – H

[1] The MUD is defined as $\frac{\sum_i^n |x_B - x_T|}{n}$ with x_B and x_T being the values as observed by Baur and in this study, respectively for the quantities of interest (i.e., bond-length and angle).

299 bonds as applied by Baur (1962) are very close to the values we observed in rozenite. Although
300 the constraints used by Baur (1962) yielded H – O distances in close agreement with our
301 refinement, the constrained model fails for the geometry of the H – O – H molecules, as reflected
302 by a large MUD of 1.05 ° and LID of 1.80 °. Moreover, the H ••• O contacts revealed a LID of
303 0.209 Å. This failure to accurately describe the hydrogen bonding geometry is most pronounced
304 in the O_w – H ••• O angles which exhibit a MUD of 9.51 ° and LID of up to 30.80 °, reinforcing
305 the importance of neutron diffraction data in order to derive accurate geometries for the complete
306 crystal structure.

307 The hydrogen bonding system in rozenite-type compounds has been subject of intensive
308 discussions (Baur 1962, 1964, 2002; Kellersohn 1992; Held and Bohaty 2002; Anderson et al.
309 2012). Based on a long donor acceptor distance of 3.02 Å Baur (1962) suggested that no
310 intermolecular hydrogen bonding takes place for the Ow2 – H2b ••• O2 contact (Fig. 3a). More
311 recent studies on the rozenite-type compounds $ZnSO_4 \cdot 4D_2O$ (Anderson et al. 2012),
312 $MnSO_4 \cdot 4D_2O$ (Held and Bohaty 2002; Anderson et al. 2012) and $CoSO_4 \cdot 4D_2O$ (Kellersohn
313 1992) interpret H2b to partake in a three-centered interaction (i.e., a bifurcated H-bond, Ow2 –
314 H2b ::: O2/O2') with long donor-acceptor distances of 3.02 Å and 3.26 Å (Fig. 3b). Kellersohn
315 (1992) investigated the Ow2 hydrogen bond system based on bond-valance considerations and
316 noted that exclusion of the two long hydrogen bonds results in the O2 atom exhibiting a
317 deficiency of 0.22 valence units. Our own bond valance calculations (Brown and Altermatt 1985;
318 Brese and O'Keeffe 1991; Alig et al. 1994) for rozenite (supplementary information; Tab. s1)
319 yield a deficiency of 0.10 valence units on the O2 atom, reducing to 0.054 if the intermolecular
320 contacts are included in the calculations. Clearly, the long intermolecular hydrogen bonds play a
321 vital role in achieving charge neutrality for the O2 atom and thus should not be neglected when

This is the peer-reviewed, final accepted version for American Mineralogist, published by the Mineralogical Society of America.
The published version is subject to change. Cite as Authors (Year) Title. American Mineralogist, in press.
DOI: https://doi.org/10.2138/am-2022-8502. http://www.minsocam.org/

describing the hydrogen bond network. Supporting this evidence in favor of a three-centered hydrogen bond in rozenite-type compounds, Anderson et al. (2012) suggested, based on an exhaustive comparison with numerous hydrogen bonding systems, that not only the H2b, but also the H3a atom is involved in a three-centered hydrogen bond (Ow3 – H3a ::: O4/Ow4) (Fig. 3c). According to our bond valance calculations the H3a ••• Ow4 contact exhibits a valency of 0.017, making it a weak but non-negligible hydrogen bond. Furthermore, when assessing the geometry of Ow3 – H3a ••• Ow4 contact (i.e., H3a ••• Ow4 = 2.425(5) Å; ∠ (Ow3 - H3a ••• Ow4) = 124.0(3) ° at 290 K) it is evident that this bond falls well within even the conservatively defined limits of hydrogen bonding (i.e., H ••• O < 3 Å; ∠ (Ow - H ••• O) = 110 ° - 180 °; (Steiner 2002)). Therefore, based on the large range of evidence in favor of three-centered hydrogen bonding involving the H3a and H2b atoms, we have adopted the hydrogen bonding system proposed by Anderson et al. (2012) (Fig. 3c) for our study.

Low temperature crystallography, thermal expansion, and absence of phase transition

The powder diffraction data revealed no splitting of Bragg peaks nor appearance of new peaks that might be indicative of a phase transition. Consequently, the refined lattice parameters also varied smoothly (Fig. 4, Tab. s3, Tab. s4). It is noteworthy that the β angle decreased systematically on cooling such that, at ~ 137 K, the unit-cell became metrically orthorhombic. However, β continued to decrease < 90 ° below 137 K and it is important to emphasize that the Laue symmetry of the diffraction pattern retains its monoclinic character throughout the whole temperature range under investigation. Thus, rozenite does not undergo any structural phase transition down to at least 21 K.

There are various approaches to quantify the temperature dependency of the lattice parameters of crystalline solids, with varying degrees of usefulness and capability for accurate extrapolation. These range from polynomial fits through to parameterizations based on the classical Einstein model of the internal energy and the more accurate Debye-type model, which is used here.

The Debye model is derived from the Grüneisen relation of the thermoelastic properties.

$$\gamma = \frac{\alpha_V V K_0}{C_V} \qquad (1)$$

where γ is the Grüneisen ratio, α_V is the volume thermal expansion coefficient, K_0 is the isothermal bulk modulus, C_V is the isochoric specific heat capacity, and V the unit-cell volume. Equation (1) is integrated with respect to the temperature, whereby γ and K_0 are assumed to be independent of the temperature. This yields the first order approximation to the Grüneisen zero pressure equation of state which expresses the thermal expansion of the crystal as a function of its internal energy $U(T)$ and isothermal bulk modulus K_0

This is the peer-reviewed, final accepted version for American Mineralogist, published by the Mineralogical Society of America.
The published version is subject to change. Cite as Authors (Year) Title. American Mineralogist, in press.
DOI: https://doi.org/10.2138/am-2022-8502. http://www.minsocam.org/

$$V(T) = V_0\left(1 + \frac{U(T)}{Q}\right) \qquad (2)$$

where $Q = (V_0 K_0/\gamma)$.

U(T) may be derived by the Debye approximation

$$U(T) = 9Nk_BT\left(\frac{T}{\theta_D}\right)^3 \int_0^{\theta_D/T} \frac{x^3}{e^x - 1} dx \qquad (3)$$

where N is the number of atoms per formula unit, k_B is Boltzmann's constant, θ_D is the Debye temperature, and $x = \hbar\omega/k_BT$. Note that the zero-point energy of $9Nk_B\theta_D/8$ is included in Equation (2) via the term V_0.

It was apparent from the residuals obtained from fitting this model to V(T) that the first-order Grüneisen model failed to provide an accurate description of the thermal expansion (see supplementary Fig. s2). Consequently, we fitted a second-order approximation to the Grüneisen zero pressure equation of state (Equation (4)), which introduces the first derivative of the bulk modulus K_0' with respect to pressure via the parameter *b*

$$V(T) = V_0\left(1 + \frac{U(T)}{Q - bU(T)}\right) \qquad (4)$$

where $b = \frac{1}{2}(K_0' - 1)$.

The sum of squared residuals is thus reduced from 0.32 $Å^6$ for the first-order fit to 0.014 $Å^6$ for the second order model.

The value of K_0/γ obtained from the second-order model is 84.5(4) GPa, increased from K_0 = 58.4(7) GPa in the poorer first-order fit. We note that Meusburger et al. (2019) obtained a bulk modulus of 45.2(2) GPa for szomolnokite ($FeSO_4 \cdot H_2O$). It is highly unlikely that rozenite, featuring isolated cyclic $[Fe(H_2O)_4SO_4]_2$ units loosely interconnected by intermolecular hydrogen bonds, exceeds the stiffness of szomolnokite featuring a rigid three dimensional

framework structure. Fortes et al. (2006) report a bulk modulus of 21.5(1) GPa for epsomite ($MgSO_4 \cdot 7H_2O$), a mineral featuring isolated $Mg(H_2O)_6$ and SO_4 units loosely interconnected by hydrogen bonds. We should expect, therefore that rozenite will exhibit a compressibility intermediate between these hydrates, implying $\gamma = 1.9 - 4.0$. We further note that an extremely large value for *K'* of 41.1 as obtained from the second-order Debye fit clearly is unphysical but typical of the case where the complexity of the underlying phonon spectrum is represented by a simple model characterized with a single Debye frequency cut-off. The parameters derived from the second order single Debye fits are given in Tab. 4 and from the first order single Debye model in the supplementary material (Tab. s2). In order to be dimensionally correct, the individual lattice parameters were fitted as a^3, b^3 and c^3.

For a more detailed assessment of the thermal expansion of rozenite the orientation and magnitude of the principal axes (Fig. 5a), and components (Fig. 5b) of the thermal expansion tensor were calculated using the Win_strain software (Angel 2011). Strain tensors were computed incrementally between consecutive data points using the finite Lagrangian strain definition. The reference temperatures correspond to the average of the temperatures of the two data points used to calculate the strains. The thermal expansion tensor is constrained to have the α_2 principal axis parallel to [010], and α_1 and α_3 lying in the (010) plane. The orientation of the crystallographic axes relative to the cartesian reference system as specified by the Institute of Radio Engineers (i.e., X || a^*; Z || c) was used for all calculations.

Cross-sections through the representation surface of the thermal expansion tensor, evaluated at 285 K (Fig. 6), allow us to understand the relationship to both the monoclinic lattice vectors and the underlying structural elements. The expansion parallel with the *a* and *c* directions of the crystal are similar. The thermal expansion || *b,* however, is substantially larger (i.e., $\alpha_a : \alpha_b$:

This is the peer-reviewed, final accepted version for American Mineralogist, published by the Mineralogical Society of America.
The published version is subject to change. Cite as Authors (Year) Title. American Mineralogist, in press.
DOI: https://doi.org/10.2138/am-2022-8502. http://www.minsocam.org/

α_c = 1.00 : 2.19 : 1.60 at 285 K). This behavior may be attributed to a large structural 'void' and the absence of hydrogen bonding between the rigid cyclic dimer units || *b* enabling the structure to undergo greater expansion in this direction upon heating (Fig. 6a).

Mapping of the thermal expansion onto the crystallographic reference frame conceals the true extent of the anisotropy, manifested in the eigenvalues and eigenvectors of the expansion tensor, i.e., the principal thermoelastic strains, $\alpha_1 : \alpha_2 : \alpha_3 = -1.00 : 3.74 : 5.40$ at 285 K. The principal axis α_1, which is approximately oriented parallel to the $\langle 101 \rangle$ direction (*a* ∠ 40.6(3) ° *b* ∠ 90 ° *c* ∠ 49.8(3) °), exhibits negative thermal expansion over the entire temperature range under investigation. Contrary to this behavior, α_3, oriented approximately || $\langle 10\bar{1} \rangle$ (*a* ∠ 49.4(3) ° *b* ∠ 90 ° *c* ∠ 139.8(3) °) is the true direction of maximum thermal expansion. The stark contrast between the negative thermal expansion approximately || $\langle 101 \rangle$ and the direction of maximum expansion approximately || $\langle 10\bar{1} \rangle$ originates from the evolution of β with temperature. Shrinkage of β, the angle spanning the $\langle 100 \rangle$ and $\langle 001 \rangle$ directions, is mirrored by a simultaneous increase of the complementary angle spanning the $\langle 100 \rangle$ and $\langle 00\bar{1} \rangle$ directions (Fig. 6b). From a structural perspective an angle β close to 90 ° results in adjacent cyclic dimers being almost perfectly stacked on top of each other both in the *a* and *c* direction, despite this is not being a requirement imposed by symmetry. The evolution of β may then be explained as being due to a subtle displacement of the cyclic dimers relative to each other as a function of temperature (Fig. 6b.). Furthermore, the distances between the central atoms of the diagonally opposing $FeO_2(H_2O)_4$ and SO_4 units (Fig. 6b), are increasing upon cooling from 9.91385(3) Å (290 K) to 9.92414(3) Å (21 K) in the $\langle 101 \rangle$ direction (i.e., approximately || α_1) and shrinking from 9.98531(3) Å (290 K) to 9.90118(3) Å (21 K) in the $\langle 10\bar{1} \rangle$ (i.e., approximately || α_3). Lastly, the

This is the peer-reviewed, final accepted version for American Mineralogist, published by the Mineralogical Society of America.
The published version is subject to change. Cite as Authors (Year) Title. American Mineralogist, in press.
DOI: https://doi.org/10.2138/am-2022-8502. http://www.minsocam.org/

relatively smaller thermal expansion in the *a* than the *c* direction (Fig. 6c) may be attributed to a denser population of the dimer units in this direction.

Comparing these findings to other hydrated sulfate minerals it is evident that both large thermoelastic anisotropy and negative linear thermal expansion in particular is a rather common phenomenon in such materials. Negative linear expansion has been observed in epsomite ($MgSO_4 \cdot 7H_2O$) (Fortes et al. 2006), meridianiite ($MgSO_4 \cdot 11H_2O$) (Fortes et al. 2008), and most recently several members of the kieserite group ($M^{2+}SO_4 \cdot H_2O$ with M^{2+} = Mg, Fe, Co, Ni) (Wildner et al. 2022). The negative thermal expansion found in our study is smaller than in $MgSO_4 \cdot 7H_2O$, $MgSO_4 \cdot H_2O$, $FeSO_4 \cdot H_2O$, $CoSO_4 \cdot H_2O$ and of approximately the same magnitude as in $NiSO_4 \cdot H_2O$ and $MgSO_4 \cdot 11H_2O$ (Tab. 5). The volume thermal expansion of rozenite is intermediate between values found in the higher hydrates (e.g., $MgSO_4 \cdot 7H_2O$ and $MgSO_4 \cdot 11H_2O$) and in the lower hydrates (e.g., $FeSO_4 \cdot H_2O$ and $MgSO_4 \cdot H_2O$) (Tab. 5).

These trends in the volume thermal expansion reflect the changing degree of polymerization of the $M^{2+}O_x(H_2O)_{6-x}$ and SO_4 units as a function of hydration state, n, changing from isolated polyhedra (n = 6 to 11) through cyclic dimers and chains (n = 3 to 5) to rigid 3D corner-sharing frameworks (n = 1).

Vibrational properties of rozenite and absence of phase transition

Hydrated sulfate minerals may de- or rehydrate under changing relative humidity conditions. Thus, it is possible that a sample or a fraction might transform after its identity and phase purity is confirmed by X-ray diffraction and any subsequent measurements may not reflect the original state. Fig. 7(a, b) displays a comparison of the Raman spectra as observed by Chio et al. (2007) and in this study, both inside and outside the glass capillary. Although the background is increased for the measurement performed through the borosilicate glass, a comparison with

447 data collected outside of the capillary demonstrates that no additional sharp bands that might be
448 mistaken for Raman-active vibrational modes appear in the spectrum (Fig. 7a).

449 Synchrotron X-ray diffraction analysis performed on the capillary sample confirms the
450 phase purity of the material (Fig. 7c). As for the data collected by Chio et al. (2007), these
451 authors noted that a shoulder at 1018 cm^{-1} observed in their Raman spectra likely originate from
452 szomolnokite impurities. A comparison of the Raman spectra collected in this study in and
453 outside of the glass capillary shows the absence of the 1018 cm^{-1} band for phase pure rozenite
454 (Fig. 7b), thus confirming this hypothesis. For this reason, acquiring Raman spectra and
455 performing X-ray diffraction on the same capillary, appears to be a suitable workflow in order to
456 produce reliable fingerprint spectra for salt hydrate phases whose hydration state is susceptible to
457 changes in relative humidity.

458 The neutron diffraction results clearly demonstrate the absence of any structural phase
459 transition down to at least 21 K. This raises the question of how the vibrational mode splitting
460 observed by Chio et al. (2007) may be explained. To understand this problem, we have computed
461 the spatial frequencies of the Raman-active vibrational modes of rozenite from first principles
462 (Fig. 8).

463 DFT predicts a total of 16 Raman-active vibrational modes in the region of the H_2O
464 stretching modes (Fig. 8a). Therefore, assuming the occurrence of vibrational mode splitting and
465 consequently a structural phase transition is not necessary in order to explain the 10 bands
466 evidenced by Chio et al. (2007) at temperatures lower than 90 K. We further note that our
467 computation suggests that several of the water stretching modes are overlapping; thus merely 10
468 instead of the total of 16 Raman-active modes are resolvable even at temperatures as low as 8 K.

469 The same holds true for the putative splitting of a mode located in the spectral region of
470 the external vibrations (Fig. 8b) where our ab initio calculations also predict two Raman-active
471 vibrational modes as closely spaced as 2.9 cm^{-1}. Therefore, we conclude that the putative
472 splitting of vibrational modes is a misinterpretation of the sharpening of these modes upon
473 cooling.

474 Both our DFT calculations as well as group theoretical analysis within the C_{2h} point
475 group using the SAM tool (Kroumova et al. 2003) as implemented in the Bilbao Crystallographic
476 Server (Aroyo et al. 2006) predict a total of 108 Raman active modes ($54A_g + 54B_g$). Since first
477 principle calculations at the Γ-point also yield the frequency of the IR-active modes as well as of
478 the acoustic phonon modes we further note that rozenite exhibits 105 IR active optical modes
479 ($53A_u + 52B_u$) as well as 3 ($A_u + 2B_u$) acoustic phonon modes, totaling to 216 phonon modes of
480 which 213 may be assigned to the optical branch and 3 to the acoustic one. The frequency and
481 symmetry for each of the Raman (Tab. s5) and IR-active (Tab. s6) vibrational modes computed
482 from first principles are provided in the supplementary material. Ruggiero et al. (2015) have also
483 modelled the vibrational properties of rozenite from first principles and curiously reported a total
484 of 213 IR-active vibrational modes (Table S3 in supplementary material of Ruggiero et al.
485 (2015)), at odd with both our first principles calculations as well as our group theoretical
486 analysis. Based on the very low intensity reported for several modes i.e., of the 32 modes in the
487 O – H stretching region 16 exhibit an intensity of less than 5% of the strongest IR active O – H
488 stretching mode, and a total number of 213 IR-active modes which corresponds to the number of
489 optical modes obtained in our study, we believe that Ruggiero et al. (2015) computed the Γ-point
490 frequencies of the complete set of optical vibrational modes but wrongly assigned them all to be
491 IR-active. Comparing the vibrational frequencies of the O – H stretching modes obtained by

Ruggiero et al. (2015) (i.e., 3451.2 – 3807.3 cm^{-1}) and the ones computed in our study (3278.7 – 3635.3 cm^{-1}) to the experimental values (3252 – 3582 cm^{-1}), it is evident that our calculations predict the vibrational mode frequencies much more accurately. Ruggiero et al. (2015) computed the vibrational frequencies at a higher level of theory and substantially higher computational cost using the B3LYP hybrid functional, yet again proving the effectiveness of the self-consistent DFT + U approach (Kulik et al. 2006; Timrov et al. 2021) in accurately predicting the material properties of transition metal compounds at a fraction of the computational cost.

Implications

We have demonstrated, by combining neutron diffraction with ab initio calculation within the framework of DFT, that the known monoclinic phase of rozenite is structurally stable over the entire temperature range it might be exposed to on the martian surface and does not undergo any structural phase transition down to temperatures of at least 21 K. Rozenite is amongst the most promising candidates for the polyhydrated sulfate phase on the martian surface. Constraining the low temperature stability and vibrational fingerprint of candidate phases such as rozenite is of vital importance to understand both the climatological history as well as for the future colonization of Mars. Characterization of the stratigraphic sequence (i.e., sulfate vs clay mineral layers) of the polyhydrated sulfate deposits may enable us to decipher the nature, drivers and onset of changing environmental conditions during the planet's early history.

As for the future colonization of Mars, hydrated sulfate minerals may be a valuable resource in the equatorial region where water ice is unstable (Feldman et al. 2004). Therefore, it is not only important to merely delineate between various mineral families, but a detailed mineralogical phase identification, including the mineral's hydration state, is crucial. For instance, 321 mL of water may be extracted from one kg rozenite, whereas complete dehydration

of the same amount of the monohydrate yields 106 mL. Moreover, rozenite may be dehydrated to szomolnokite at 315 K, producing 241 mL H_2O/kg, whereas complete desiccation of szomolnokite to anhydrous $FeSO_4$ takes place at much higher temperature (approximately 500 K) (Kanari et al. 2018). In contrast, the dehydration of rozenite to szomolnokite is more efficient process, thus making it a potentially valuable resource for the extraction of water on Mars.

Raman spectroscopy has proven to be a very effective tool in discriminating between the various hydrated mineral species (Košek et al. 2017), but such efficacy relies on an accurate spectral library of the most promising candidate phases. As part of the scientific payload of the Perseverance rover the first two Raman spectrometer were successfully deployed on the martian surface (Bhartia et al. 2021; Wiens et al. 2020). The European Space Agency's Rosalind Franklin Rover (Rull et al. 2017), which is expected to land on the martian surface in 2023, will also rely on Raman spectroscopy for mineralogical phase identification. Accurate vibrational fingerprint data is becoming increasingly important in planetary exploration. In our study, we have demonstrated that the challenges associated with the sensitivity of the sample material to changing relative humidity conditions may be circumvented by analyzing the sample inside a glass capillary and performing synchrotron X-ray diffraction on the very same capillary. Lastly, we want to highlight the role DFT may play in vibrational mode assignment and interpretation, in particular at low-temperatures where sharpening of vibrational modes might be misinterpreted as mode splitting. This will become even more important in the future as computational resources become cheaper and more readily available, and likewise quantum chemical codes become increasingly user friendly and optimized for high-throughput calculations. Combining such calculations with experimentally determined reference spectra will enable the construction of a reliable Raman spectroscopic database for planetary exploration, which will be invaluable to

538 shed light on the geological past as well as in identifying resources for the future colonization of
539 planetary bodies in the solar system.

540 Acknowledgment

541 We want to thank STFC's Scientific Computing Department for the provision of
542 computing resources on the SCARF cluster and in particular Jon Roddom for compiling the
543 Quantum ESPRESSO code. Moreover, we want to thank two anonymous reviewers for their
544 thorough reading and constructive feedback. We further acknowledge the STFC for access to
545 beamtime at the ISIS Neutron and Muon Source (RB2010354) and the Diamond Light Source
546 (CY26409). JMM acknowledges funding from an ISIS Facility Development and Utilisation
547 Studentship (50 %) and the University of Exeter (50 %).

548 References

549 Albinati, A., and Willis, B.T.M. (1982) The Rietveld method in neutron and X-ray powder
550 diffraction. Journal of Applied Crystallography, 15, 361–374.

551 Alig, H., Losel, J., and Trömel, M. (1994) Zur Kristallchemie der Wasserstoff–Sauerstoff-
552 Bindungen. Zeitschrift für Kristallographie - Crystalline Materials, 209, 18–21.

553 Amadon, B., Jollet, F., and Torrent, M. (2008) γ and β cerium: LDA+U calculations of ground-
554 state parameters. Physical Review B, 77, 155104.

555 Anderson, J.L., Peterson, R.C., and Swainson, I. (2012) The atomic structure of deuterated
556 boyleite $ZnSO_4 \cdot 4D_2O$, ilesite $MnSO_4 \cdot 4D_2O$, and bianchite $ZnSO_4 \cdot 6D_2O$. American
557 Mineralogist, 97, 1905–1914.

558 Angel, R.J. (2011) Win_Strain4. Padova.

559 Aroyo, M.I., Perez-Mato, J.M., Capillas, C., Kroumova, E., Ivantchev, S., Madariaga, G., Kirov,
560 A., and Wondratschek, H. (2006) Bilbao Crystallographic Server: I. Databases and

561 crystallographic computing programs. Zeitschrift für Kristallographie - Crystalline
562 Materials, 221, 15–27.
563 Baur, W.H. (1962) Zur Kristallchemie der Salzhydrate. Die Kristallstrukturen von $MgSO_4.4H_2O$
564 (leonhardtit) und $FeSO_4.4H_2O$ (rozenit). Acta Crystallographica, 15, 815–826.
565 ——— (1964) On the crystal chemistry of salt hydrates. II. A neutron diffraction study of
566 $MgSO_4.4H_2O$. Acta Crystallographica, 17, 863–869.
567 ——— (1972) Prediction of hydrogen bonds and hydrogen atom positions in crystalline solids.
568 Acta Crystallographica Section B, 28, 1456–1465.
569 ——— (2002) Zinc(II) sulfate tetrahydrate and magnesium sulfate tetrahydrate. Addendum.
570 Acta Crystallographica Section E, 58, e9–e10.
571 Bhartia, R., Beegle, L.W., DeFlores, L., Abbey, W., Razzell Hollis, J., Uckert, K., Monacelli, B.,
572 Edgett, K.S., Kennedy, M.R., Sylvia, M., and others (2021) Perseverance's Scanning
573 Habitable Environments with Raman and Luminescence for Organics and Chemicals
574 (SHERLOC) Investigation. Space Science Reviews, 217, 58.
575 Bibring, J.-P., Langevin, Y., Gendrin, A., Gondet, B., Poulet, F., Berthé, M., Soufflot, A.,
576 Arvidson, R., Mangold, N., Mustard, J., and others (2005) Mars Surface Diversity as
577 Revealed by the OMEGA/Mars Express Observations. Science, 307, 1576–1581.
578 Bibring, J.-P., Langevin, Y., Mustard, J., Poulet, F., Arvidson, R., Gendrin, A., Gondet, B.,
579 Mangold, N., Berthé, M., Gomez, C., and others (2006) Global Mineralogical and Aqueous
580 Mars History Derived from OMEGA/Mars Express Data. Science (New York, N.Y.), 312,
581 400–404.
582 Bishop, J.L., Parente, M., Weitz, C.M., Noe Dobrea, E.Z., Roach, L.H., Murchie, S.L., McGuire,
583 P.C., McKeown, N.K., Rossi, C.M., Brown, A.J., and others (2009) Mineralogy of Juventae

584 Chasma: Sulfates in the light-toned mounds, mafic minerals in the bedrock, and hydrated
585 silica and hydroxylated ferric sulfate on the plateau. Journal of Geophysical Research:
586 Planets, 114.
587 Brese, N.E., and O'Keeffe, M. (1991) Bond-valence parameters for solids. Acta
588 Crystallographica Section B, 47, 192–197.
589 Brown, I.D., and Altermatt, D. (1985) Bond-valence parameters obtained from a systematic
590 analysis of the Inorganic Crystal Structure Database. Acta Crystallographica Section B, 41,
591 244–247.
592 Carter, J., Poulet, F., Bibring, J.-P., Mangold, N., and Murchie, S. (2013) Hydrous minerals on
593 Mars as seen by the CRISM and OMEGA imaging spectrometers: Updated global view.
594 Journal of Geophysical Research: Planets, 118, 831–858.
595 Chio, C., Sharma, S., and Muenow, D. (2007) The hydrates and deuterates of ferrous sulfate
596 ($FeSO_4$): A Raman spectroscopic study. Journal of Raman Spectroscopy, 38, 87–99.
597 Cococcioni, M., and de Gironcoli, S. (2005) Linear response approach to the calculation of the
598 effective interaction parameters in the LDA + U method. Physical Review B, 71, 35105.
599 Dudarev, S.L., Botton, G.A., Savrasov, S.Y., Humphreys, C.J., and Sutton, A.P. (1998) Electron-
600 energy-loss spectra and the structural stability of nickel oxide: An LSDA+U study.
601 Physical Review B, 57, 1505–1509.
602 Feldman, W., Mellon, M., Maurice, S., Prettyman, T., Carey, B., Vaniman, D., Bish, D., Claire,
603 F., Chipera, S., Kargel, J., and others (2004) Hydrated states of $MgSO_4$ at equatorial
604 latiudes on Mars. Geophysical Research Letters, 31, L16702-4.

605 Floris, A., de Gironcoli, S., Gross, E.K.U., and Cococcioni, M. (2011) Vibrational properties of
606 MnO and NiO from DFT + U-based density functional perturbation theory. Physical
607 Review B, 84, 161102.
608 Floris, A., Timrov, I., Himmetoglu, B., Marzari, N., de Gironcoli, S., and Cococcioni, M. (2020)
609 Hubbard-corrected density functional perturbation theory with ultrasoft pseudopotentials.
610 Physical Review B, 101, 64305.
611 Fortes, A.D., Wood, I.G., Alfredsson, M., Vočadlo, L., and Knight, K.S. (2006) The
612 thermoelastic properties of $MgSO_4 \cdot 7D_2O$ (epsomite) from powder neutron diffraction and
613 ab initio calculation. European Journal of Mineralogy, 18, 449–462.
614 Fortes, A.D., Wood, I., and Knight, K. (2008) The crystal structure and thermal expansion tensor
615 of $MgSO_4 \cdot 11D_2O$(meridianiite) determined by neutron powder diffraction. Physics and
616 Chemistry of Minerals , 35, 207–221.
617 Garrity, K.F., Bennett, J.W., Rabe, K.M., and Vanderbilt, D. (2014) Pseudopotentials for high-
618 throughput DFT calculations. Computational Materials Science, 81, 446–452.
619 Giannozzi, P., Baroni, S., Bonini, N., Calandra, M., Car, R., Cavazzoni, C., Ceresoli, D.,
620 Chiarotti, G.L., Cococcioni, M., Dabo, I., and others (2009) QUANTUM ESPRESSO: a
621 modular and open-source software project for quantum simulations of materials. Journal of
622 Physics: Condensed Matter, 21, 395502.
623 Giannozzi, P., Andreussi, O., Brumme, T., Bunau, O., Buongiorno Nardelli, M., Calandra, M.,
624 Car, R., Cavazzoni, C., Ceresoli, D., Cococcioni, M., and others (2017) Advanced
625 capabilities for materials modelling with Quantum ESPRESSO. Journal of Physics:
626 Condensed Matter, 29, 465901.

627 Gómez-Elvira, J., Armiens, C., Carrasco, I., Genzer, M., Gómez, F., Haberle, R., Hamilton, V.E.,
628 Harri, A.-M., Kahanpää, H., Kemppinen, O., and others (2014) Curiosity's rover
629 environmental monitoring station: Overview of the first 100 sols. Journal of Geophysical
630 Research: Planets, 119, 1680–1688.
631 Greenspan, L. (1977) Humidity Fixed Points of Binary Saturated Aqueous Solutions. Journal of
632 Research of the National Bureau of Standards. Section A, Physics and Chemistry, 81A, 89–
633 96.
634 Grimme, S. (2006) Semiempirical GGA-type density functional constructed with a long-range
635 dispersion correction. Journal of Computational Chemistry, 27, 1787–1799.
636 Held, P., and Bohaty, L. (2002) Manganese(II) sulfate tetrahydrate (ilesite). Acta
637 Crystallographica Section E, 58, i121–i123.
638 Hohenberg, P., and Kohn, W. (1964) Inhomogeneous Electron Gas. Physical Review, 136,
639 B864–B871.
640 Hudson-Edwards, K.A., Schell, C., and Macklin, M.G. (1999) Mineralogy and geochemistry of
641 alluvium contaminated by metal mining in the Rio Tinto area, southwest Spain. Applied
642 Geochemistry, 14, 1015–1030.
643 Jambor, J., Nordstrom, D., and Alpers, C. (2000) Metal-sulfate Salts from Sulfide Mineral
644 Oxidation. Reviews in Mineralogy and Geochemistry, 40, 303–350.
645 Kanari, N., Menad, N.-E., Ostrosi, E., Shallari, S., Diot, F., Allain, E., and Yvon, J. (2018)
646 Thermal Behavior of Hydrated Iron Sulfate in Various Atmospheres. Metals, 8.
647 Kellersohn, T. (1992) Structure of cobalt sulfate tetrahydrate. Acta Crystallographica Section C,
648 48, 776–779.

649 Klingelhöfer, G., Morris, R. v, Bernhardt, B., Schröder, C., Rodionov, D.S., de Souza, P.A., Yen,
650 A., Gellert, R., Evlanov, E.N., Zubkov, B., and others (2004) Jarosite and Hematite at
651 Meridiani Planum from Opportunity's Mössbauer Spectrometer. Science, 306, 1740.
652 Kohn, W., and Sham, L.J. (1965) Self-Consistent Equations Including Exchange and Correlation
653 Effects. Physical Review, 140, A1133–A1138.
654 Košek, F., Culka, A., Drahota, P., and Jehlička, J. (2017) Applying portable Raman
655 spectrometers for field discrimination of sulfates: Training for successful extraterrestrial
656 detection. Journal of Raman Spectroscopy, 48, 1085–1093.
657 Kroumova, E., Aroyo, M.I., Perez-Mato, J.M., Kirov, A., Capillas, C., Ivantchev, S., and
658 Wondratschek, H. (2003) Bilbao Crystallographic Server : Useful Databases and Tools for
659 Phase-Transition Studies. Phase Transitions, 76, 155–170.
660 Kulik, H.J., Cococcioni, M., Scherlis, D.A., and Marzari, N. (2006) Density Functional Theory
661 in Transition-Metal Chemistry: A Self-Consistent Hubbard U Approach. Physical Review
662 Letters, 97, 103001.
663 Langevin, Y., Poulet, F., Douté, S., Vincendon, M., Bibring, J.-P., Gondet, B., Forget, F.,
664 Montmessin, F., and Schmitt, B. (2006) The Vis/NIR OMEGA imaging spectrometer on-
665 board Mars Express.
666 Meusburger, J.M., Ende, M., Talla, D., Wildner, M., and Miletich, R. (2019) Transformation
667 mechanism of the pressure-induced C2/c-to-$P1^{-}$ transition in ferrous sulfate monohydrate
668 single crystals. Journal of Solid State Chemistry, 277.
669 Meusburger, J.M., Hudson-Edwards, K.A., Tang, C.C., Crane, R.A., and Fortes, A.D. (2021)
670 Elasticity of selected icy satellite candidate materials (CO_2, C_6H_6, $MgSO_4 \cdot 7H_2O$ and
671 $CaSO_4 \cdot 2H_2O$) revisited by dispersion corrected density functional theory. Icarus, 114611.

672 Meusburger, J.M., Hudson-Edwards, K.A., Tang, C.T., Connolly, E.T., Crane, R.A., and Fortes,
673 A.D. (2022) Low-temperature crystallography and vibrational properties of rozenite
674 ($FeSO_4 \cdot 4H_2O$), a candidate mineral component of the polyhydrated sulfate deposits on
675 Mars. Materials Cloud Archive.
676 Mitchell, A.G. (1984) The preparation and characterization of ferrous sulphate hydrates. Journal
677 of Pharmacy and Pharmacology, 36, 506–510.
678 Momma, K., and Izumi, F. (2011) VESTA3 for three-dimensional visualization of crystal,
679 volumetric and morphology data. Journal of Applied Crystallography, 44, 1272–1276.
680 Monkhorst, H.J., and Pack, J.D. (1976) Special points for Brillouin-zone integrations. Phys. Rev.
681 B, 13, 5188–5192.
682 Nordstrom, D. (2011) Mine Waters: Acidic to Circmneutral. Elements, 7.
683 Perdew, Burke, and Ernzerhof (1996) Generalized Gradient Approximation Made Simple.
684 Physical review letters, 77 18, 3865–3868.
685 Pfrommer, B.G., Cote, M., Louie, S.G., and Cohen, M.L. (1997) Relaxation of crystals with the
686 quasi-Newton method. Journal of Computational Physics, 131, 233–240.
687 Raczkowski, D., Canning, A., and Wang, L.W. (2001) Thomas-Fermi charge mixing for
688 obtaining self-consistency in density functional calculations. Physical Review B, 64,
689 121101.
690 Roach, L.H., Mustard, J.F., Swayze, G., Milliken, R.E., Bishop, J.L., Murchie, S.L., and
691 Lichtenberg, K. (2010) Hydrated mineral stratigraphy of Ius Chasma, Valles Marineris.
692 Icarus, 206, 253–268.
693 Rohatgi, A. (2021) Webplotdigitizer: Version 4.5.

694 Ruggiero, M.T., Bardon, T., Strlič, M., Taday, P.F., and Korter, T.M. (2015) The role of
695 terahertz polariton absorption in the characterization of crystalline iron sulfate hydrates.
696 Physical Chemistry Chemical Physics, 17, 9326–9334.
697 Rull, F., Maurice, S., Hutchinson, I., Moral, A., Perez, C., Diaz, C., Colombo, M., Belenguer, T.,
698 Lopez-Reyes, G., Sansano, A., and others (2017) The Raman Laser Spectrometer for the
699 ExoMars Rover Mission to Mars. Astrobiology, 17, 627–654.
700 Squyres, S.W., Grotzinger, J.P., Arvidson, R.E., Bell, J.F., Calvin, W., Christensen, P.R., Clark,
701 B.C., Crisp, J.A., Farrand, W.H., Herkenhoff, K.E., and others (2004) In Situ Evidence for
702 an Ancient Aqueous Environment at Meridiani Planum, Mars. Science, 306, 1709.
703 Steiner, T. (2002) The Hydrogen Bond in the Solid State. Angewandte Chemie International
704 Edition, 41, 48–76.
705 Talla, D., and Wildner, M. (2019) Investigation of the kieserite–szomolnokite solid-solution
706 series, (Mg,Fe)$SO_4 \cdot H_2O$, with relevance to Mars: Crystal chemistry, FTIR, and Raman
707 spectroscopy under ambient and martian temperature conditions. American Mineralogist,
708 104, 1732–1749.
709 Thompson, S.P., Parker, J.E., Potter, J., Hill, T.P., Birt, A., Cobb, T.M., Yuan, F., and Tang, C.C.
710 (2009) Beamline I11 at Diamond: A new instrument for high resolution powder diffraction.
711 Review of Scientific Instruments, 80, 075107.
712 Timrov, I., Marzari, N., and Cococcioni, M. (2018) Hubbard parameters from density-functional
713 perturbation theory. Physical Review B, 98, 85127.
714 ——— (2021) Self-consistent Hubbard parameters from density-functional perturbation theory
715 in the ultrasoft and projector-augmented wave formulations. Physical Review B, 103,
716 45141.

Toby, B.H. (2001) EXPGUI, a graphical user interface for GSAS. Journal of Applied Crystallography, 34, 210–213.

Tosca, N.J., McLennan, S.M., Clark, B.C., Grotzinger, J.P., Hurowitz, J.A., Knoll, A.H., Schröder, C., and Squyres, S.W. (2005) Geochemical modeling of evaporation processes on Mars: Insight from the sedimentary record at Meridiani Planum. Earth and Planetary Science Letters, 240, 122–148.

van Laar, B., and Schenk, H. (2018) The development of powder profile refinement at the Reactor Centre Netherlands at Petten. Acta Crystallographica Section A, 74, 88–92.

Wang, A., Jolliff, B.L., Liu, Y., and Connor, K. (2016) Setting constraints on the nature and origin of the two major hydrous sulfates on Mars: Monohydrated and polyhydrated sulfates. Journal of Geophysical Research: Planets, 121, 678–694.

Wiens, R.C., Maurice, S., Robinson, S.H., Nelson, A.E., Cais, P., Bernardi, P., Newell, R.T., Clegg, S., Sharma, S.K., Storms, S., and others (2020) The SuperCam Instrument Suite on the NASA Mars 2020 Rover: Body Unit and Combined System Tests. Space Science Reviews, 217, 4.

Wildner, M., Zakharov, B.A., Bogdanov, N.E., Talla, D., Boldyreva, E. v, and Miletich, R. (2022) Crystallography relevant to Mars and Galilean icy moons: crystal behavior of kieserite-type monohydrate sulfates at extraterrestrial conditions down to 15 K. IUCrJ, 9.

Tables

Crystal data		
Chemical Formula	$FeSO_4 \cdot 4D_2O$	$FeSO_4 \cdot 4D_2O$
Space group	$P2_1/n$	$P2_1/n$
Temperature	290 K	21 K
a, b, c, β	5.966031(12) Å, 13.609756(31) Å, 7.962529(14) Å, 90.4288(2) °	5.942863(15) Å, 13.521390(40) Å, 7.933688(20) Å, 89.8617(2) °
V	646.509(2)	637.516(2)
Z	4	4
Refinement		
R-factors goodness of fit	Rp = 0.0237, Rwp = 0.0179, χ^2 = 2.190	Rp = 0.0316, Rwp = 0.0257, χ^2 = 5.472
Number of refined parameters	192	182*

Tab. 1. Selected details of the crystal structure refinement, for a full description we refer to the CIF. *Number of refined parameters is lower for the measurement at 21 K since the background coefficients had to be fixed for the 30 – 130 ms TOF window.

Source	**Baur**	**This study**	**Diff***	**This study**	**Diff****
T (K)	RT	290		21	
Fe-O1	2.120(9)	2.121(3)	-0.001	2.130(3)	-0.009
Fe-O2	2.120(9)	2.130(3)	-0.010	2.127(3)	0.003
Fe-Ow1	2.099(11)	2.096(3)	0.003	2.108(3)	-0.011
Fe-Ow2	2.129(11)	2.139(4)	-0.010	2.145(3)	-0.006
Fe-Ow3	2.127(11)	2.114(4)	0.013	2.113(3)	-0.001
Fe-Ow4	2.126(11)	2.097(3)	0.029	2.094(3)	0.003
MSiD[1]			0.004		-0.003
MUD			0.011		0.006
O1-Fe-Ow1	86.2(2.4)	87.44(11)	-1.24	87.44(10)	0.00
O1-Fe-Ow2	95.7(2.4)	95.51(12)	0.19	95.50(11)	0.01
O1-Fe-Ow3	87.0(2.4)	87.13(12)	-0.13	86.88(10)	0.25
O1-Fe-O2	91.9(2.4)	91.00(10)	0.90	90.81(10)	0.19
Ow4-Fe-Ow1	85.5(2.4)	84.73(12)	0.77	84.36(11)	0.37
Ow4-Fe-Ow2	92.5(2.4)	92.31(13)	0.19	92.69(12)	-0.38
Ow4-Fe-Ow3	92.5(2.4)	92.64(13)	-0.14	92.86(11)	-0.22
Ow4-Fe-O2	88.8(2.4)	89.17(12)	-0.37	89.48(11)	-0.31
Ow1-Fe-Ow3	90.7(2.4)	91.97(13)	-1.27	92.47(11)	-0.50
Ow2-Fe-O2	94.0(2.4)	93.10(12)	0.90	93.33(11)	-0.23
Ow2-Fe-Ow3	86.8(2.4)	87.35(13)	-0.55	86.56(11)	0.79
MSiD			-0.068		-0.003
MUD			0.605		0.295
S-O1	1.512(8)	1.487(5)	0.025	1.478(5)	0.009
S-O2	1.492(8)	1.482(5)	0.010	1.485(5)	-0.003
S-O3	1.488(8)	1.468(5)	0.002	1.484(5)	-0.016
S-O4	1.473(8)	1.481(5)	-0.008	1.481(6)	0.000
MSiD			0.012		-0.003
MUD			0.016		0.007
O1-S-O2	109.4(1.1)	108.2(3)	1.2	109.7(4)	-1.5
O1-S-O3	108.3(1.1)	110.4(3)	-2.1	109.9(3)	0.5
O1-S-O4	108.3(1.1)	108.7(3)	-0.4	109.0(3)	-0.3
O2-S-O3	109.7(1.1)	109.3(3)	0.4	108.3(3)	1.0
O2-S-O4	111.8(1.1)	111.2(3)	0.6	111.0(3)	0.2
O3-S-O4	109.3(1.1)	109.0(3)	0.3	108.9(4)	0.1
MSiD			-0.24		0.3
MUD			0.76		0.42

Tab. 2. Bond lengths and angles for the octahedral and tetrahedral units as determined in this study at 290 K and 21 K and compared to the values reported by Baur (1962). * refers to the difference between Baur and this

This is the peer-reviewed, final accepted version for American Mineralogist, published by the Mineralogical Society of America.
The published version is subject to change. Cite as Authors (Year) Title. American Mineralogist, in press.
DOI: https://doi.org/10.2138/am-2022-8502. http://www.minsocam.org/

study's 290 K structure. ** refers to the difference of this study's 290 K and 21 K structures, thus elucidating the influence of temperature on the respective quantity. [1]The Mean signed difference is defined as $\frac{\sum_i^n x_B - x_T}{n}$ with x_B and x_T being the values as observed by Baur and in this study, respectively for the quantities of interest (i.e., bond-length and angle).

Source	**Baur**	**This study**	**Diff***	**This study**	**Diff****
T (K)	RT	290		21	
Ow1-H1a	1.010(8)	0.947(5)	0.063	0.965(5)	-0.018
Ow1-H1b	0.962(9)	0.962(4)	0.000	0.972(4)	-0.01
Ow2-H2a	0.933(9)	0.963(5)	-0.03	0.959(4)	0.004
Ow2-H2b	0.958(9)	0.944(5)	0.014	0.975(4)	-0.031
Ow3-H3a	0.955(8)	0.950(5)	0.005	0.949(4)	0.001
Ow3-H3b	0.975(9)	0.943(4)	0.032	0.962(4)	-0.019
Ow4-H4a	0.960(8)	0.953(5)	0.007	0.968(4)	-0.015
Ow4-H4b	0.964(9)	0.973(4)	-0.009	0.960(4)	0.013
MSiD			0.010		-0.009
MUD			0.020		0.014
H1a-Ow1-H1b	105.2(8)	106.0(4)	-0.80	107.8(4)	-1.80
H2a-Ow2-H2b	104.0(8)	105.5(5)	-1.50	107.1(4)	-1.6
H3a-Ow3-H3b	110.2(8)	108.4(4)	1.80	108.1(4)	0.3
H4a-Ow4-H4b	105.1(8)	105.0(4)	0.10	106.9 (4)	-1.90
MSiD			-0.10		-1.25
MUD			1.05		1.40
Ow1-O3	2.855(10)	2.898(4)	-0.043	2.848(4)	0.050
Ow1-O3'	2.790(10)	2.764(4)	0.026	2.744(4)	0.020
Ow2-O4	2.867(10)	2.858(4)	0.009	2.834(4)	0.024
Ow2-O2	3.023(10)	3.015(4)	0.008	2.986(4)	0.029
Ow2-O2'	3.267(10	3.274(4)	-0.007	3.250(4)	0.024
Ow3-O4	2.845(10)	2.836(4)	0.009	2.794(4)	0.042
Ow3-Ow4	3.025(12)	3.059(5)	-0.034	3.029(4)	0.030
Ow3-O1	2.805(10)	2.816(4)	-0.011	2.795(4)	0.021
Ow4-O4	2.837(10)	2.848(4)	-0.011	2.832(4)	0.016
Ow4-O3	2.723(10)	2.733(4)	-0.010	2.718(4)	0.015
MSiD			-0.0064		0.027
MUD			0.0168		0.027
H1a-O3	1.865(6)	1.957(4)	-0.092	1.888(4)	0.069
H1b-O3'	1.834(6)	1.808(4)	0.026	1.776(4)	0.032
H2a-O4	2.201(6)	1.992(5)	0.209	1.967(4)	0.025
H2b-O2	2.417(6)	2.330(5)	0.087	2.249(4)	0.081
H2b-O2'	2.593(6)	2.551(4)	0.042	2.525(4)	0.026
H3a-O4	2.113(6)	2.015(4)	0.098	1.974(4)	0.041
H3a-Ow4	2.345(9)	2.425(5)	-0.080	2.399(4)	0.026
H3b-O1	1.833(6)	1.874(4)	-0.041	1.834(4)	0.040
H4a-O4	1.969(6)	1.948(4)	0.021	1.918(4)	0.093
H4b-O3	1.899(6)	1.764(4)	0.135	1.764(4)	0.000
MSiD			0.041		0.037
MUD			0.083		0.037
O3-Ow1-O3'	104.8(4)	104.90 (11)	-0.10	104.46(10)	0.44
O4-Ow2-O2	144.5(4)	143.43(14)	1.07	142.81(12)	0.62
O4-Ow2-O2'	92.6(3)	93.12(11)	-0.52	93.75(9)	-0.63
O4-Ow3-O1	137.2(4)	136.23(13)	0.97	135.54(11)	0.69
Ow4-Ow3-O1	70.8(3)	70.28(10)	0.52	69.45(8)	0.83
O4-Ow4-O3	117.3(4)	116.68(12)	0.62	118.30(11)	-1.62
MSiD			0.43		0.055
MUD			0.63		0.805
Ow1-H1a-O3	165.8(5)	172.0(4)	-6.2	173.5(4)	-1.60
Ow1-H1b-O3'	171.8(6)	172.5(4)	-0.7	173.1(4)	-0.60
Ow2-H2a-O4	125.7(6)	148.5(4)	-22.8	149.2(3)	-0.70
Ow2-H2b-O2	122.6(6)	129.0(4)	-6.4	131.5(3)	-2.50
Ow2-H2b-O2'	129.6(6)	133.6(4)	-4.0	131.0(3)	2.60
Ow3-H3a-O4	132.3(6)	143.6(3)	-11.3	143.4(3)	0.20
Ow3-H3a-Ow4	127.7(6)	124.0(3)	3.7	123.6(3)	0.40

This is the peer-reviewed, final accepted version for American Mineralogist, published by the Mineralogical Society of America.
The published version is subject to change. Cite as Authors (Year) Title. American Mineralogist, in press.
DOI: https://doi.org/10.2138/am-2022-8502. http://www.minsocam.org/

Ow3-H3b-O1	173.7(5)	175.4(4)	-1.7	176.0(3)	-0.6
Ow4-H4a-O4	149.2(6)	156.7(4)	-7.5	156.4(3)	0.3
Ow4-H4b-O3	141.8(5)	172.6(4)	-30.8	172.2(3)	0.4
MSiD			-8.77		-0.2
MUD			9.51		0.98

Tab. 3. Geometry of the hydrogen bonds as determined in this study at 290 K and 21 K, and compared to the values reported by Baur (1962). *refers to the difference between Baur and this study's 290 K structure. ** refers to the difference of this study's 290 K and 21 K structures, thus elucidating the influence of temperature on the respective quantity.

	a^3	b^3	c^3	β	V
θ_D (K)	240(6)	303(2)	382(4)	381(13)	278(2)
X_0 (cm^3 mol^{-1})	31.5994(6)	372.182(2)	75.1823(4)	13.5290(4)	95.9829(4)
X_0 (Å, $Å^3$)	5.9428(1)	13.5214(8)	7.9337(5)	934(19)	637.533(3)
Q (x10^4 J cm^{-3})	850(15)	519(3)	1047(12)	1263(26)	811.(3)
K_0/γ (GPa)	269(5)	13.94(7)	139(2)	1617(17)	84.5(4)
K'	12.6	19.92	90.76	146.55	41.11

Tab. 4. Parameters derived from fitting a second order single Debye model upon the lattice parameters of rozenite.

Compound	**NTE (K^{-1})**	**T_{ref}**	**VTE expansion (K^{-1})**	**T_{ref} (K)**	**Source**
$MgSO_4 \cdot 11H_2O$	–1.2(5) x 10^{-5}	50	6.8(4) x 10^{-5}	240	Fortes et al. (2008)
$MgSO_4 \cdot 7H_2O$	–2.0(2) x 10^{-5}	125	10.8(3) x 10^{-5}	290	Fortes et al. (2006)
$FeSO_4 \cdot 4H_2O$	–1.0(2) x 10^{-5}	285	8.2(5) x 10^{-5}	285	This study
$MgSO_4 \cdot H_2O$	–4.4(3) x 10^{-5}	293	3.4(7) x 10^{-5}	293	Wildner et al. (2022)
$FeSO_4 \cdot H_2O$	–1.7(2) x 10^{-5}	293	4.7(5) x 10^{-5}	293	Wildner et al. (2022)
$CoSO_4 \cdot H_2O$	–2.7(2) x 10^{-5}	293	3.3(3) x 10^{-5}	293	Wildner et al. (2022)
$NiSO_4 \cdot H_2O$	–0.8(5) x 10^{-5}	293	3.6(4) x 10^{-5}	293	Wildner et al. (2022)

Tab.5. Comparison of the negative (NTE) and volume (VTE) thermal expansion of various $M^{2+}SO_4 \cdot nH_2O$.

Figures

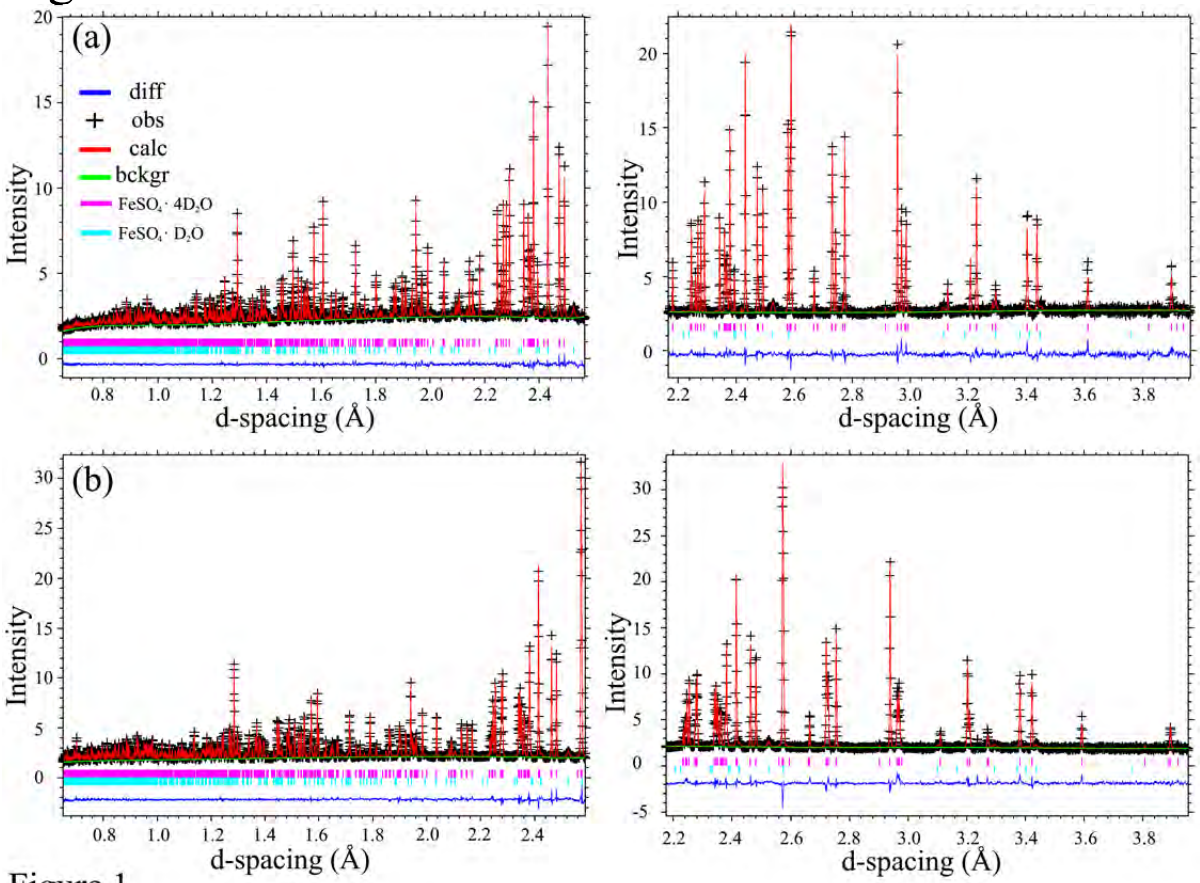

Figure 1

Fig. 1. Neutron diffraction patterns acquired at (a) 290 K and (b) 21 K in the backscattering detector bank collected in the 30 – 130 (left) and 100 – 200 ms (right) TOF window. The observed data plotted as crosses, the red line represents the fitted model, and the blue line the difference profile. The tick marks corresponding to each of the Bragg peaks of $FeSO_4 \cdot 4D_2O$ and $FeSO_4 \cdot D_2O$ are displayed in magenta and cyan, respectively.

This is the peer-reviewed, final accepted version for American Mineralogist, published by the Mineralogical Society of America.
The published version is subject to change. Cite as Authors (Year) Title. American Mineralogist, in press.
DOI: https://doi.org/10.2138/am-2022-8502. http://www.minsocam.org/

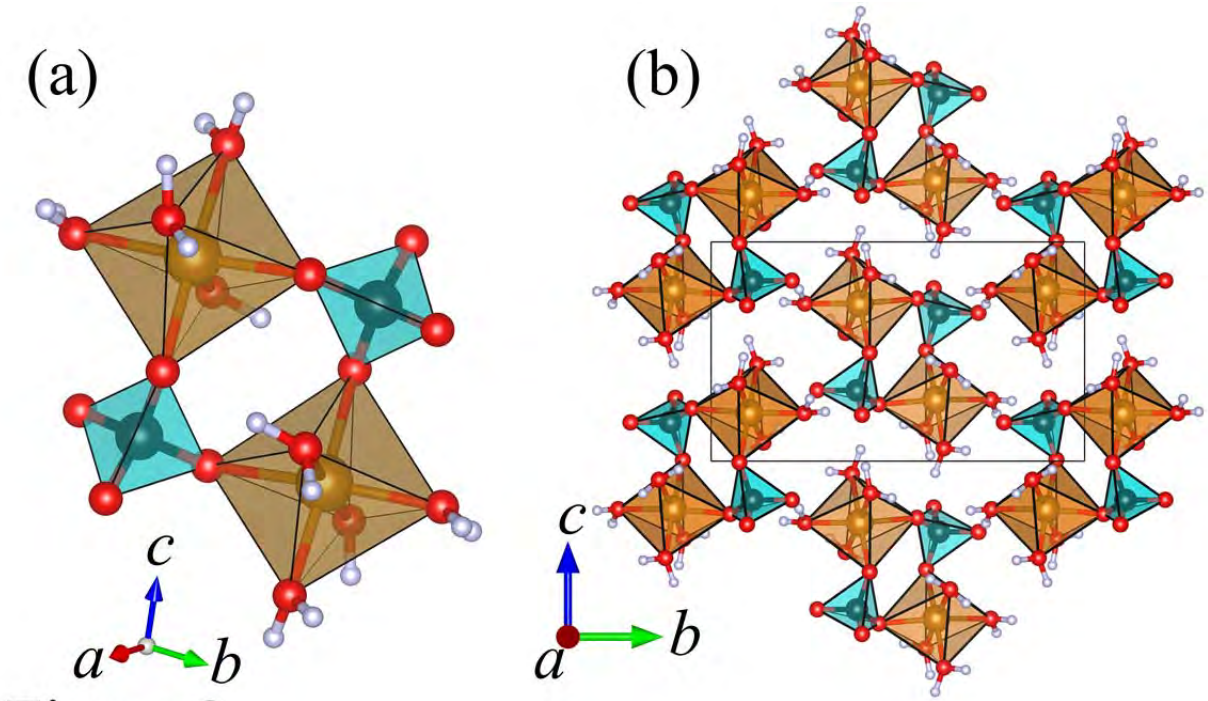

Figure 2

776

777 Fig. 2. Crystal structure of rozenite drawn using the VESTA software (Momma and Izumi 2011). (a) Detailed
778 view of the $[Fe(H_2O)_4SO_4]_2$ units. Note that the non-hydrated oxygens of the $Fe(H_2O)_4O_2$ units form bridges to
779 the SO_4 tetrahedra (orange and cyan, respectively). (b) The $[Fe(H_2O)_4SO_4]_2$ isolated units are linked via a
780 complex network of intermolecular hydrogen bonds.
781

This is the peer-reviewed, final accepted version for American Mineralogist, published by the Mineralogical Society of America.
The published version is subject to change. Cite as Authors (Year) Title. American Mineralogist, in press.
DOI: https://doi.org/10.2138/am-2022-8502. http://www.minsocam.org/

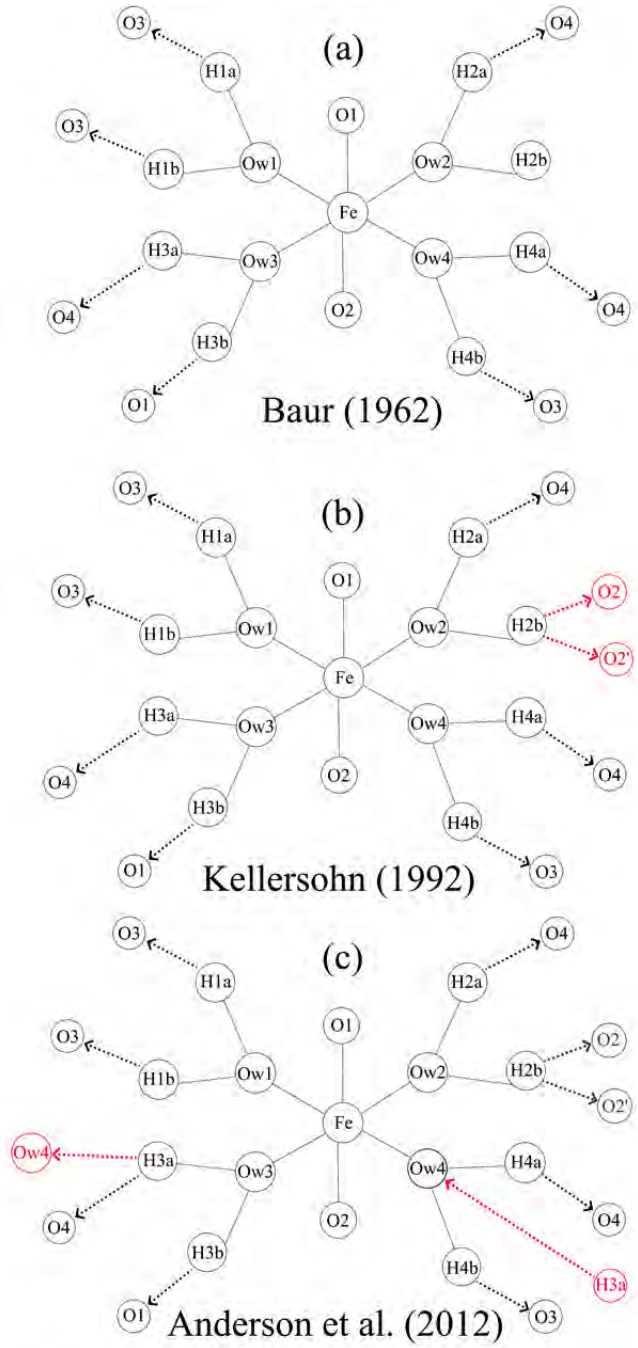

Figure 3

Fig. 3 Interpretation of the hydrogen bond network by (a) Baur (1962), (b) Kellersohn (1992) and (c) Anderson et al. (2012). The changes suggested by these authors with respect to the previous interpretation are marked in red.

This is the peer-reviewed, final accepted version for American Mineralogist, published by the Mineralogical Society of America.
The published version is subject to change. Cite as Authors (Year) Title. American Mineralogist, in press.
DOI: https://doi.org/10.2138/am-2022-8502. http://www.minsocam.org/

789

790

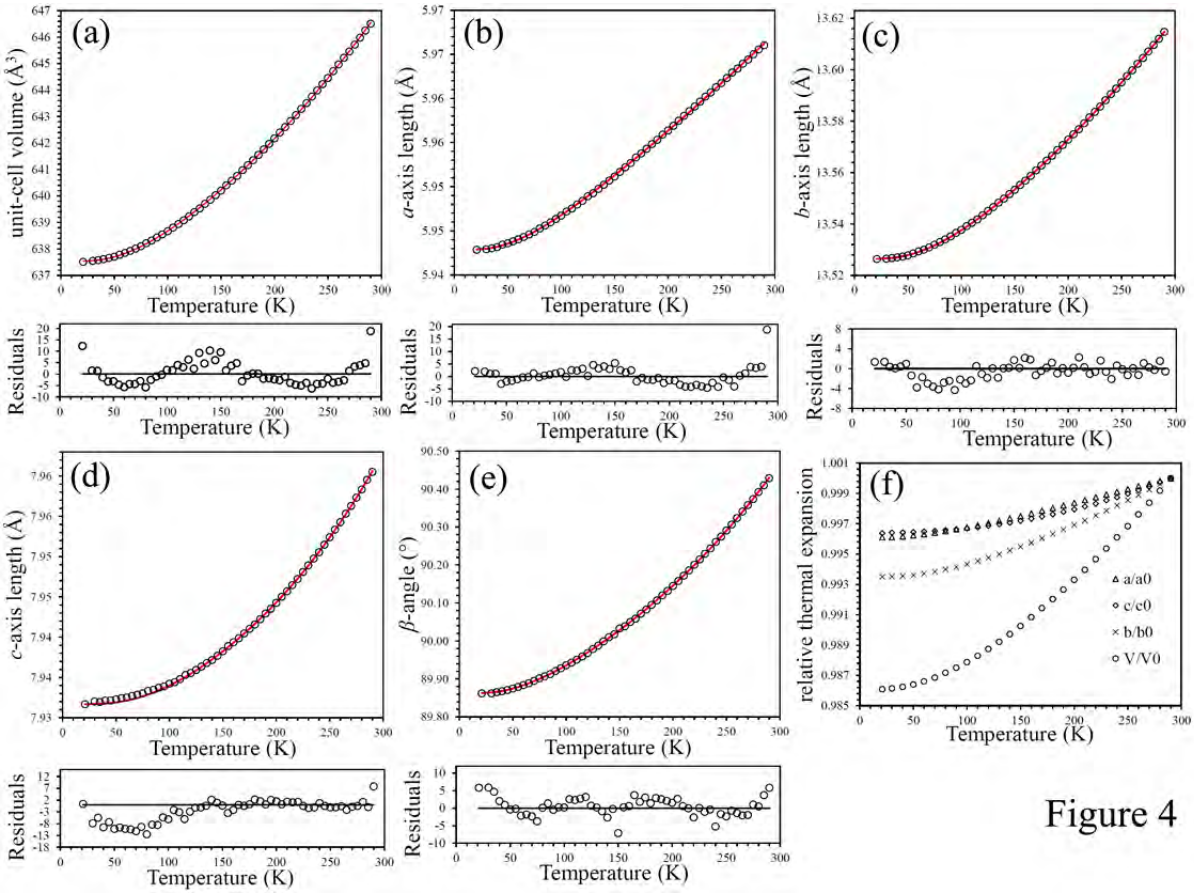

Figure 4

791

792 Fig. 4. (a-e) Second-order Debye model fit (red line) to the lattice parameters (black open circle) of rozenite in
793 at temperatures ranging from 290 to 21 K. Error bars are smaller than the symbol size. Residuals are defined
794 as the difference between observed and fitted values divided by the experimental estimated standard deviation
795 determined for each data point. (f) Relative thermal expansion of each of the lattice parameters as a function of
796 temperature. Note the crossover in the evolution of the *a* and *c* axes (T ~ 100 K).

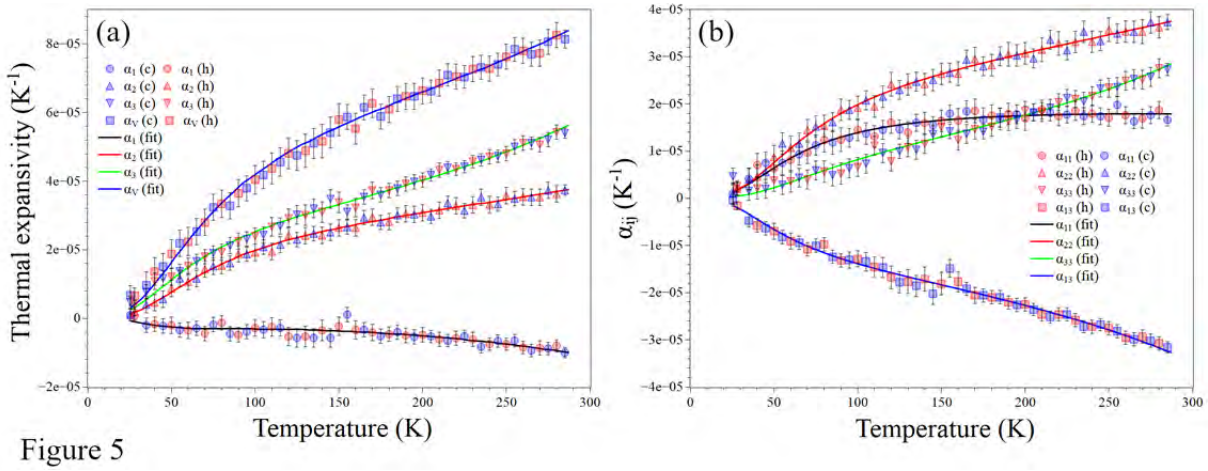

Figure 5

797

This is the peer-reviewed, final accepted version for American Mineralogist, published by the Mineralogical Society of America.
The published version is subject to change. Cite as Authors (Year) Title. American Mineralogist, in press.
DOI: https://doi.org/10.2138/am-2022-8502. http://www.minsocam.org/

Fig. 5. The evolution of the thermal expansion tensor's the principal axes (a), and components (b) is continuous over the entire temperature range under investigation. Solid lines represent the 2nd order Debye model fit; red and blue symbols are calculated from the lattice parameter data acquired upon heating and cooling respectively. Error bars were plotted as 3σ.

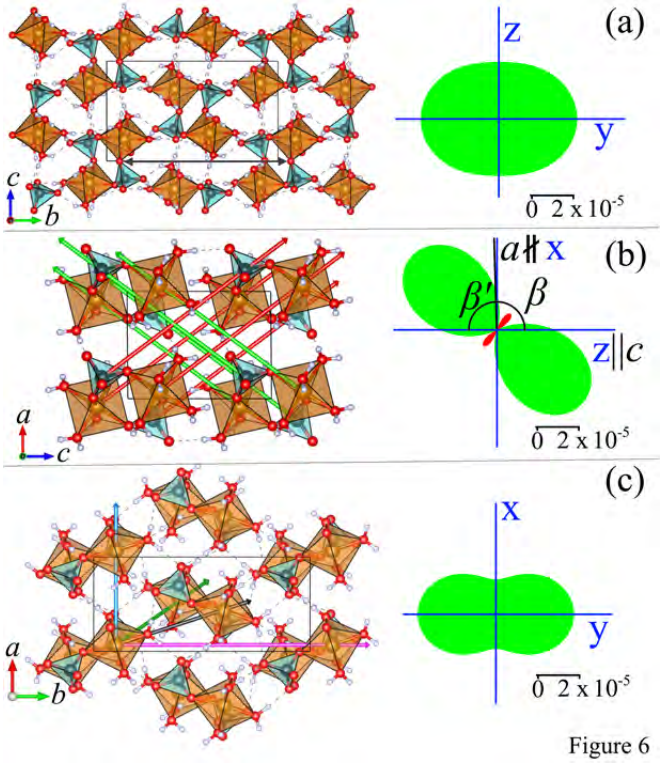

Figure 6

Fig. 6. View of the crystal structure (left) and cross-sections of the thermal expansion tensor (green represents positive, red negative values) at 285 K (right). (a) view || *a*: Large 'void' (black arrow: 11.932(5) Å at 290 K and 11.878(5) Å at 21 K) || *b* as well as absence of hydrogen bonding in this direction allows the structure to experience substantial expansion and contraction in this direction as compared to the *c*-direction. (b) view || *b*: Red arrows point || ⟨101⟩ (i.e., the direction of negative thermal expansion, whereas green arrows are oriented ⟨10$\bar{1}$⟩ (i.e., the direction of maximum thermal expansion). The cyclic dimer units are stacked on top of each other and oriented by the angle of β (~90 °). Furthermore, the distance between diagonally opposing Fe and S atoms (connected by the red and green arrows) is increasing upon cooling shrinking in the direction of maximum thermal expansion. (c) view || *c*: arrows point towards to the central atoms of the $FeO_2(H_2O)_4$ units of neighboring $FeO_2(H_2O)_4$ units.

This is the peer-reviewed, final accepted version for American Mineralogist, published by the Mineralogical Society of America.
The published version is subject to change. Cite as Authors (Year) Title. American Mineralogist, in press.
DOI: https://doi.org/10.2138/am-2022-8502. http://www.minsocam.org/

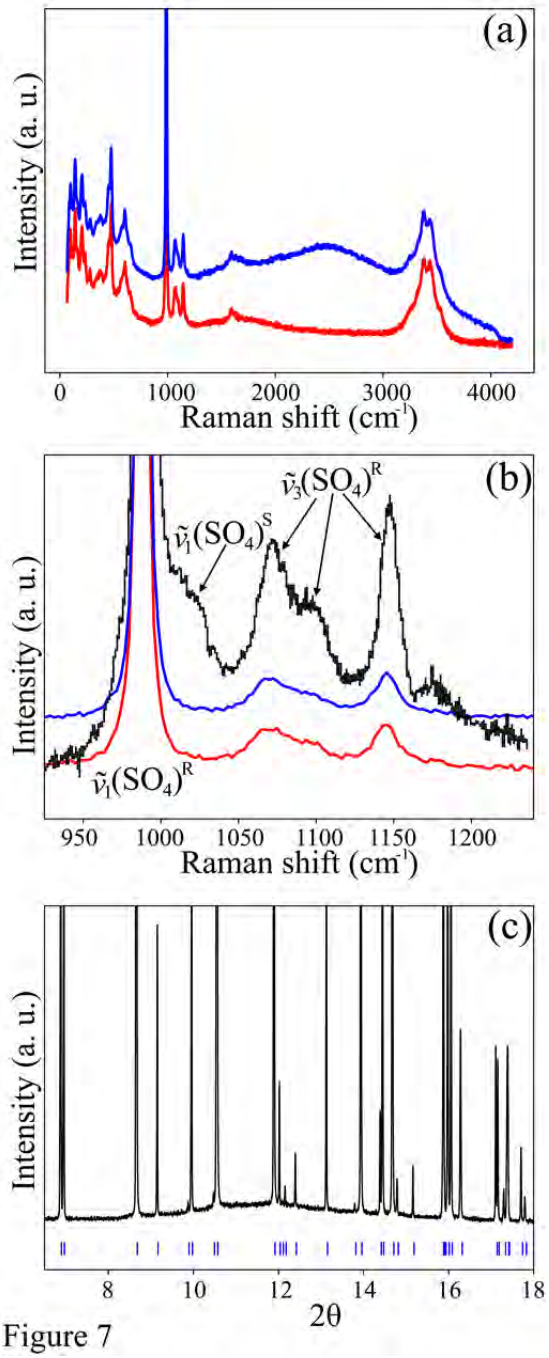

Figure 7

Fig. 7. (a) Raman spectra acquired in this study outside (red) and inside (blue) of a borosilicate glass capillary. (b) Selected spectral range for comparison between our data (red and blue curves) and Chio et al. (2007) (black curve). (c) The phase purity of our sample has been confirmed by means of synchrotron X-ray diffraction, suggesting that the shoulder at 1018 cm^{-1} in the Chio et al. (2007) spectrum (black) stems from a contamination of the sample with szomolnokite. $\tilde{\nu}(SO_4)^R$ and $\tilde{\nu}(SO_4)^S$ refer to the sulfate stretching modes assigned to rozenite and szomolnokite, respectively. The Raman spectrum reported by Chio et al. (2007) was digitized using the Webplotdigitizer tool (Rohatgi 2021). The intensity in all graphs was normalized with respect to the maximum intensity.

This is the peer-reviewed, final accepted version for American Mineralogist, published by the Mineralogical Society of America.
The published version is subject to change. Cite as Authors (Year) Title. American Mineralogist, in press.
DOI: https://doi.org/10.2138/am-2022-8502. http://www.minsocam.org/

821

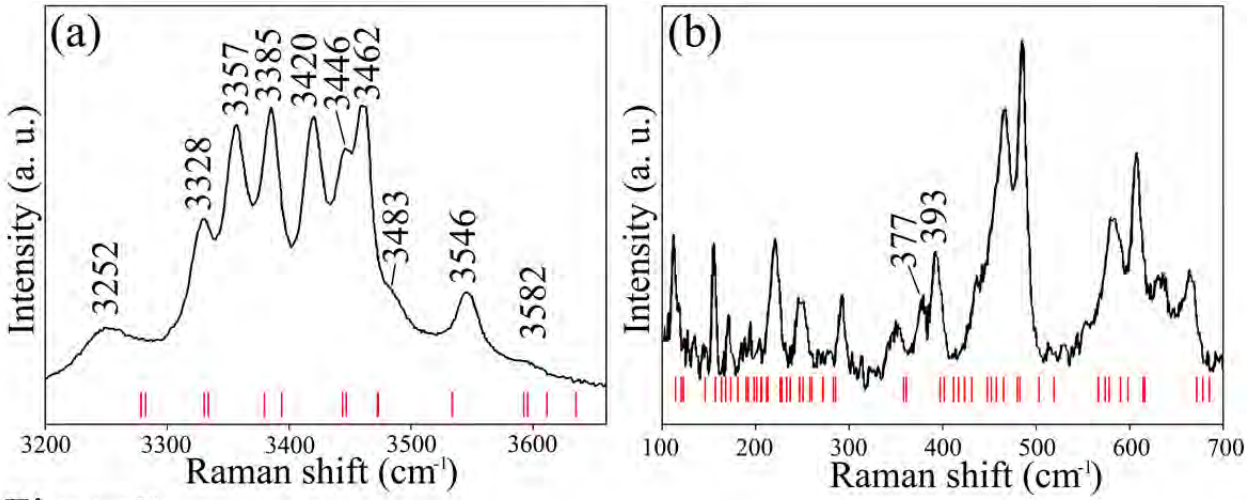

Figure 8

822 Fig. 8. Spectral region of the (a) water stretching vibration and (b) external modes of the Raman spectrum
823 acquired by Chio et al. (2007) at 8 K. Red markers indicate the Raman-active vibrational mode positions as
824 predicted by DFT. The Raman spectrum reported by Chio et al. (2007) was digitized using the
825 Webplotdigitizer tool (Rohatgi 2021).
826

827